

Analysis of TJ-II experimental data with neoclassical formulations of the radial electric field

This content has been downloaded from IOPscience. Please scroll down to see the full text.

2015 Plasma Phys. Control. Fusion 57 115004

(<http://iopscience.iop.org/0741-3335/57/11/115004>)

View [the table of contents for this issue](#), or go to the [journal homepage](#) for more

Download details:

IP Address: 132.248.29.129

This content was downloaded on 10/09/2015 at 17:44

Please note that [terms and conditions apply](#).

Analysis of TJ-II experimental data with neoclassical formulations of the radial electric field

C Gutiérrez-Tapia¹, J J Martinell², D López-Bruna³, A V Melnikov^{4,5},
L Eliseev⁴, C Rodríguez³, M A Ochando³, F Castejón³, J García⁶, B P van
Milligen³ and J M Fontdecaba³

¹ Instituto Nacional de Investigaciones Nucleares, 52045 Ocoyoacac, Edo. de México, México

² Instituto de Ciencias Nucleares-Universidad Nacional Autónoma México, México D.F., México

³ Laboratorio Nacional de Fusión, Asociación EURATOM-CIEMAT, 28040-Madrid, Spain

⁴ National Research Centre 'Kurchatov Institute', 12382 Moscow, Russia

⁵ National Research Nuclear University MEPhI, 115409 Moscow, Russia

⁶ CEA-Cadarache, 13115 Saint-Paul-lès-Durance, France

E-mail: [martinel@nucleares.unam.mx](mailto:martinell@nucleares.unam.mx)

Received 23 September 2014, revised 13 July 2015

Accepted for publication 27 July 2015

Published 10 September 2015



Abstract

Neoclassical theory provides usable expressions for studying transport in toroidal plasmas and computing the associated radial electric field. An algebraic and three semi-analytical models are used here to study the radial electric field in TJ-II plasmas and compare it with experimental data from a heavy ion beam probe (HIBP) and with DKES calculations. Good qualitative agreement as well as reasonable quantitative agreement is found which allows us to validate the models for describing TJ-II radial electric fields. Furthermore, a simple algebraic formulation (2005 *Plasma Phys. Rep.* **31** 14) provides physical insight for the interpretation of experimental data from the TJ-II heliac in spite of its complicated geometry, like the place of the transition from the electron to the ion root of the radial electric field, which occurs at the maximum value of collisionality, for example.

Keywords: stellarator TJ-II, HIBP diagnostic, plasma potential, neoclassical transport

(Some figures may appear in colour only in the online journal)

1. Introduction

The radial electric field, E_r , is generally recognized as a key factor in determining the quality of transport in stellarators and tokamaks. In both types of device there is compelling evidence that sheared $E \times B$ flows can suppress or considerably reduce the turbulence that produces large confinement losses, especially near the edge where steep E_r -gradients have been shown to play an important role in L-H transition [2]. In the case of stellarators, neoclassical (NC) collisional transport is also strongly dependent on E_r over the whole plasma column due to the nonambipolarity of particle fluxes [3]. NC transport theory has been successful in describing the phenomenology observed in stellarators and heliotrons with quite different

magnetic configurations, like the formation of an electron heat transport barrier near the magnetic axis in low-density discharges for example, the so called 'core electron root confinement' or CERC (see e.g. LHD [4], CHS [5], W7-AS [6], TJ-II [7, 8] or [9] for common features in various devices). The establishment of a radial variation of E_r is mainly determined by NC transport and the shear of $E \times B$ flows in turn modifies turbulent anomalous transport. Thus, it is generally true that E_r is a key element for understanding both anomalous and collisional transport mechanisms.

In non-axisymmetric magnetic configurations like those of stellarators, the NC contribution is crucial in the analysis of phenomena related to E_r . Indeed, there have been joint efforts to proceed to a benchmark of numerically obtained NC

electric fields and fluxes with experimental data in conditions suitable for an NC treatment [10]. In the particular case of the TJ-II device, an acceptable agreement between experiments and Monte Carlo calculations has been obtained in low density regimes [11, 12]. For this reason, some works were started to compare a particular formulation of NC fluxes to describe the electric fields with experiments in restricted plasma conditions [13, 14]. These and other later exercises encourage the use of any formulation that preserves the main neoclassical scalings of electron and ion radial fluxes to obtain the radial electric field. For example, measurements in the T-10 tokamak and the TJ-II stellarator could be qualitatively explained using collisional transport to calculate the electric field, thus suggesting the ambipolar nature of turbulent fluxes in these two devices [15]. Similarly, simple neoclassical descriptions of transport could be used to describe experimental trends in non-axisymmetric toroidal devices of differing magnetic geometry [16].

Since the conditions and basic statements of NC theory are well grounded and provide a first approximation to transport, it is desirable to have practical implementations that evaluate this important contribution to transport and especially to the ambipolar radial electric field. The present work is also benchmark-minded, but from a more immediate and practical perspective: it is based on easy-to-implement formulations of the NC particle fluxes. The objective is to provide a practical tool for the evaluation of the radial electric field under the assumptions that (i) the main non-ambipolar radial fluxes are of neoclassical origin and (ii) the functional dependencies of such fluxes for electrons and ions are enough to obtain E_r even if the fluxes themselves are not accurately described. If the results obtained from the NC formulations are found to be consistent with the experimental results, this NC model should be suitable as a tool for the interpretation of experimental data, and also for predictive estimates. For this to be trustworthy, not one but different formulations of the NC problem should yield consistent and robust results with respect to the experimentally found trends of the radial electric field. We believe that this is especially significant when the exercise is undertaken with plasmas operated in a complex magnetic geometry like that of a Helic device, as TJ-II is. With this in mind, we organize the work as follows. First, the main characteristics of the TJ-II stellarator and the plasmas subject to this study are described in section 2. In section 3 we recall the NC models that will be used for most of the comparisons. All are variants of the basic NC approach, having particular representations, and the main purpose of the study is to show that all of them give similar predictions for E_r . A model appropriate for algebraic formulation is described and the solutions for E_r are given. Then, in section 4 after also explaining the procedure for obtaining E_r from the numerical models, radial electric field profiles are found for all the models, for a representative discharge of TJ-II that covers all density ranges of interest. For comparison purposes, E_r is also found from the kinetic code DKES which provides well accepted results. A general discussion of the behavior of E_r and the NC model with respect to density in all the plasma regimes, comparing experimental and model results, is given in section 5. Here, the algebraic formulation is

used to discuss some features of the passage from the electron to the ion root in TJ-II plasmas. Finally, section 6 summarizes the work and the conclusions are presented.

2. Experimental data

The TJ-II Helic-type stellarator has a helical magnetic axis that winds around a circumference of radius $R_0 = 1.5$ m. The plasma has a bean-shaped cross section with an average minor radius of $a \approx 0.2$ m and a magnetic field at the axis of $B_0 \approx 0.95$ T. The plasmas are initiated with electron cyclotron resonance heating (ECH); absorbed heating powers are normally $P_{ECH} = (200\text{--}400)$ kW and in the absence of other heat sources the line averaged densities are $\bar{n} = (0.3\text{--}1.0) \times 10^{19}$ m $^{-3}$ with central electron temperatures of $T_e(0) \sim 1$ keV and ion temperatures of $T_i(0) \sim 0.1$ keV due to Coulomb heat exchange. Additional heating and fueling can be obtained with the help of one or two neutral beam injectors (NBI) delivering port-through powers of $P_{NBI} = (300\text{--}700)$ kW each. Above line densities of around 1.2×10^{19} m $^{-3}$ the ECH are no longer effective and the plasmas are sustained with NBI heating alone up to densities of $\bar{n} = (2.0\text{--}6.0) \times 10^{19}$ m $^{-3}$ with lower temperatures: $T_e(0) \lesssim 0.3$ keV and $T_i(0) \sim 0.5T_e(0)$.

The electron density and temperature profiles are measured using the Thomson Scattering diagnostic from the magnetic axis up to $\rho \approx 0.7$, where ρ is the normalized flux surface label proportional to the square root of the enclosed plasma volume. In order to obtain the density profiles, atomic beam, interferometry and reflectometry data are used to extend the profiles to the edge ensuring that their line integral matches the experimental value. The ion temperature is normally measured with the CX neutrals analyzer. $T_i(\rho)$ is quite homogeneous in the low density ECH plasmas and thus very different from the T_e profiles due to the low collisional coupling in these cases. In what follows, we use T_i based on the central values provided by the diagnostic. The plasma potential in the bulk plasma is measured using the HIBP system described in [18].

The usual operation of NBI discharges consists of establishing a steady state ECH target plasma on which the NBI is launched. Owing to coating techniques based on lithiumization, the NBI phase can be sustained a with steady averaged density [19], but in this work we are interested in the variation of plasma potential profiles with density. Therefore, a discharge with a continuous density ramp has been chosen, figure 1(a). Here, the ECH (2×220 kW, nominal ECH) is maintained during the entire discharge but the NBI heating (≈ 400 kW, co-injected) starts at $t = 1070$ ms causing a slight density increment. After some delay related to NBI slowdown times, the neutral beam forces a density ramp up with decreasing T_e until the ECH cut-off density is reached at $t \approx 1120$ ms. Then T_e drops down to ~ 300 eV and the density grows until the plasma is quenched due to radiative collapse before the NBI phase ends. During the hot NBI phase, T_i becomes slightly peaked with central values that stay around 0.14 keV. Discharge #15585 in figure 1 is operated with hydrogen on the TJ-II standard magnetic configuration 100_44_64.

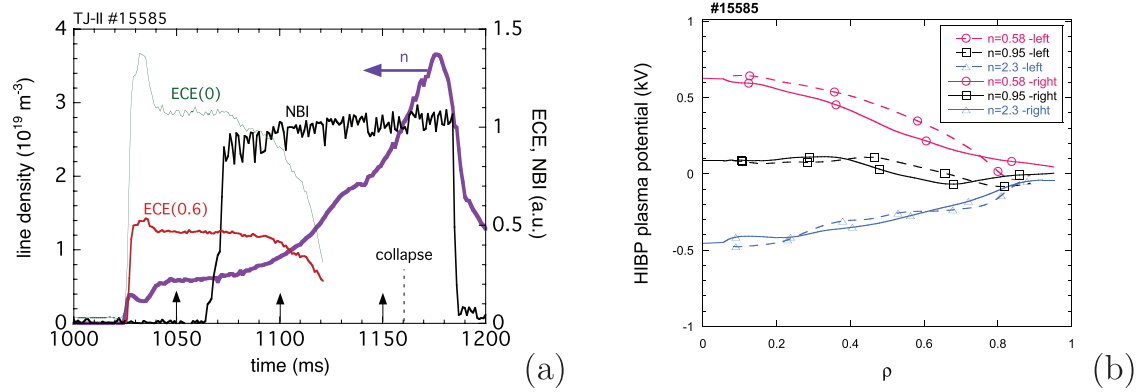


Figure 1. (a) Time signals of electron cyclotron emission (ECE) from the magnetic axis and from $\rho = 0.6$, line density \bar{n} through the magnetic axis and NBI heating during an NBI discharge (TJ-II #15585) with continuous density rise. The ECE signals drop when the ECE cut-off is reached at $\bar{n} \approx 1.2 \times 10^{19} \text{ m}^{-3}$ but the plasma remains hot until the radiative collapse at $t \approx 1160$ ms. (b) Plasma potential profiles corresponding to the times indicated with the arrows in (a).

Figure 1(b) shows the plasma potential profiles $\phi(\rho)$ that correspond to the times indicated by vertical arrows in figure 1(a) [17, 25]. Two profiles are shown at each density value because the diagnostic takes measurements at both sides of the magnetic axis (labeled ‘left’ and ‘right’). This will be used as an indication of the uncertainty in the evaluation of the plasma potential. During the ECH phase $\phi(0)$ is positive with values in the 400–1000 V range that depend on \bar{n} . At high enough densities still in the ECH phase, the plasma potential becomes negative near the plasma edge and also causes the appearance of negative electric fields around the region of the maximum density gradient [20]. In discharge #15585 this happens during the mixed ECH + NBI phase, when \bar{n} increases, T_e decreases and T_i also experiences a small ($\sim 20\%$) rise correlated to the increased density. At still larger densities, like in the pure-NBI phase, $\phi(0)$ becomes negative as in the rest of the plasma. When $\bar{n} \approx 2 \times 10^{19} \text{ m}^{-3}$, the plasma potential is negative everywhere reaching values between -300 and -600 V near the magnetic axis. It should be noted that the change in the sign of the plasma potential occurs in a rather continuous way, starting near the edge where $T_e \sim 50$ eV and moving towards the center as n increases.

In TJ-II, three different types of plasma are typically considered to represent different collisionality regimes. They can be characterized by the corresponding average electron density:

LDHT (low density with high electron temperature): low density ($\sim 0.6 \times 10^{19} \text{ m}^{-3}$), high electron temperature ($T_e(0) \sim 1$ keV) and low ion temperature ($T_i \sim 0.1$ keV) as normally found in ECH plasmas. This regime is characterized by the long mean free paths (LMFP) of the particles over most of the plasma, $\nu^* \ll 1$, giving rise to radial fluxes dominated by the contribution of bouncing trapped particles in the large magnetic ripple. Here, $\nu^* = \nu/\omega_t$ is the collision frequency normalized to a nominal transit frequency $\omega_t = v_{th}/(R_0 q) = \nu_{th}/(2\pi R_0)$, involving the rotational transform in radians ι and the thermal speed v_{th} . In this regime the electrons, being much faster than the ions and having large magnetic moment due to the heating system (ECH), dominate the radial fluxes causing E_r to be positive and $\phi \sim T_e/e$ in the

plasma core. The plasma potential is then positive over the entire plasma column.

IDT (intermediate density and electron temperature): intermediate densities ($\sim 10^{19} \text{ m}^{-3}$) and electron temperatures ($T_e(0) \sim 0.5$ keV), typically found in mixed ECH + NBI plasmas, or in high-density ECH plasmas. The electron temperatures are lower than in the typical ECH plasma, while T_i remains at the order of 0.1 keV. This regime is known from the first TJ-II experimental campaigns for inverting the sign of the plasma potential (inferred from floating potential measured with electric probes [21]), as well as the electric field (according to spectroscopic measurements of plasma rotation [22]) somewhere inside the plasma. In particular, E_r starts becoming more negative near the plasma edge [20]. With increasing average densities, the negative values of E_r also cover smaller radii.

HDLT (high density and low electron temperature): high density ($\gtrsim 2 \times 10^{19} \text{ m}^{-3}$) and low temperatures ($T_e(0) \lesssim 0.3$ keV, $T_i(0) \lesssim 0.14$ keV), corresponding to NBI plasmas. When the density is further increased from the IDT regime, the plasmas have closer electron and ion temperatures and high density giving rise to shorter mean free paths for electrons and ions, satisfying $\nu^* \lesssim 1$, ions being closer to one. The contribution from helically trapped particles is now much smaller and the radial transport in these conditions is probably dominated by passing and toroidally trapped particles over a large portion of the plasma column, which corresponds to the ‘plateau’ regime. The larger tendency of ions to escape the plasma causes $E_r < 0$ in the entire plasma column.

Figure 2 shows density (a) and electron temperature (b) profiles taken from the same experimental day of discharge #15585 (figure 1) at fixed line densities within a 10% range, with values (0.5, 1, 1.5, 2 and 2.5 in 10^{19} m^{-3} units). The profiles shown correspond to the averages of Thomson Scattering profiles based on N discharges, with $N = (6, 6, 3, 5$ and $1)$ respectively—only one discharge was available for the highest density. Each individual profile is obtained after fitting a short expansion (typically 4th or 5th order) of Bessel functions in order to obtain $T_e(\rho)$ and $n_e(\rho)$ with reasonably smooth radial derivatives. Note that Thomson

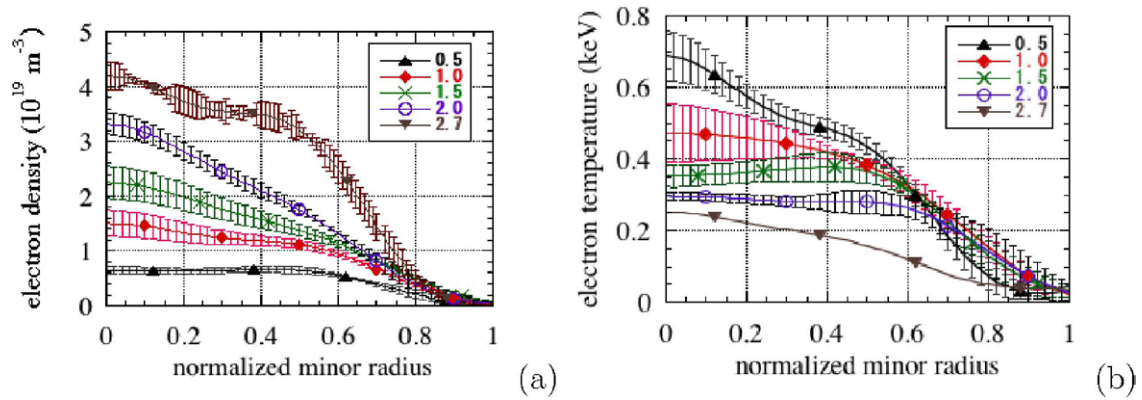


Figure 2. The averages of Thomson Scattering profiles at different line densities \bar{n} (10^{19} m^{-3}) taken from N sample discharges according to the $\bar{n}(N)$ sequence 0.5(6), 1.0(6), 1.5(3), 2.0(5), 2.7(1). Large error bars in $T_e(\rho > 0.8)$ at $\bar{n} = 2.7$ have not been drawn for clarity.

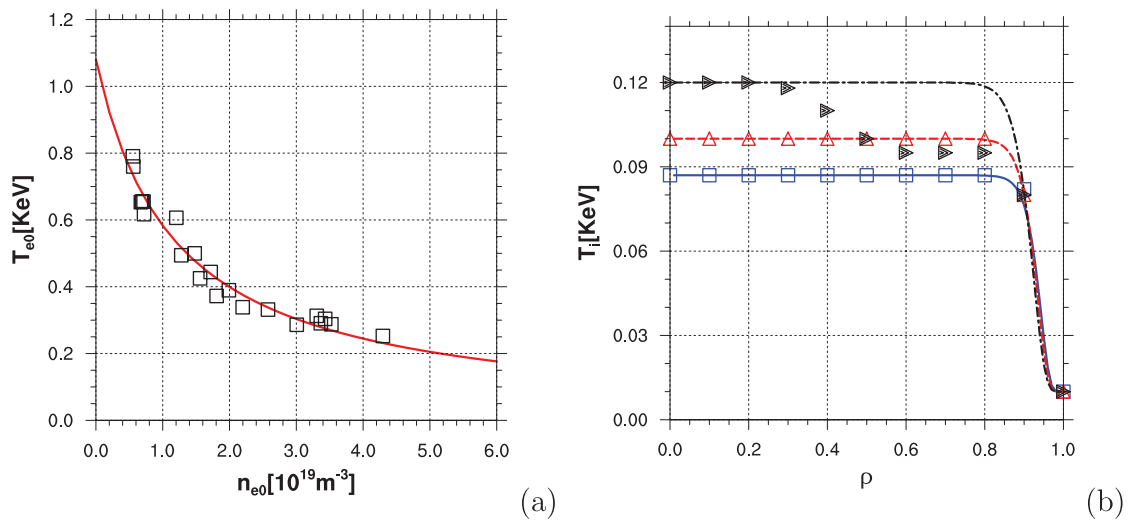


Figure 3. (a) Measured central electron temperature as a function of central density showing hyperbolic-like dependence; (b) Ion temperature: LDHT regime (solid line) and experimental (hollow-squares), IDT regime (dashed lines) and experimental (hollow-triangles), and HDLT regime (dash-dotted line) experimental (right-pointing triangles).

Scattering profiles are obtained from around 200 points in the TJ-II diagnostic giving a fine structure [23]; in the present study we are only interested in the main macroscopic variations. The error bars in figure 2 are the standard deviation of the corresponding N profiles, except for the highest density case, where the errors obtained from Bayesian analysis [24] are shown for the only available discharge. Incidentally, this shows that these two errors are similar. The profiles and their radial derivatives are then mapped to a same calculation grid $[\rho_j]$. The ion density n_i is slaved to n_e through a prescribed effective charge $Z_{\text{eff}} = 1.2$.

According to our regime classification, the curve in figure 2 labeled 0.5 in line averaged density corresponds to the LDHT regime, where we can see the rather flat $n(\rho)$ and more peaked $T_e(\rho)$. As a cautionary note, we must warn that these discharges were operated normally with off-axis ECH, which yields less peaking of T_e than the customary on-axis heating. This is in line with the notion that there is no clear temperature (nor density) profile stiffness in these plasmas. Similarly, profiles corresponding to the IDT regime fall between those labeled 1.0 and 1.5. Typical profiles for

the HDLT regime are labeled with line densities 2.0 and 2.7. The largest density in figure 2 is typical of the last stage with pure NBI heating—one injector at $\approx 400 \text{ kW}$ of port-through power—when the plasma is cooling down: $T_e(0) \approx 200 \text{ eV}$, $T_i(0) \approx 120 \text{ eV}$, $\bar{n} \approx 2.5 \times 10^{19} \text{ m}^{-3}$.

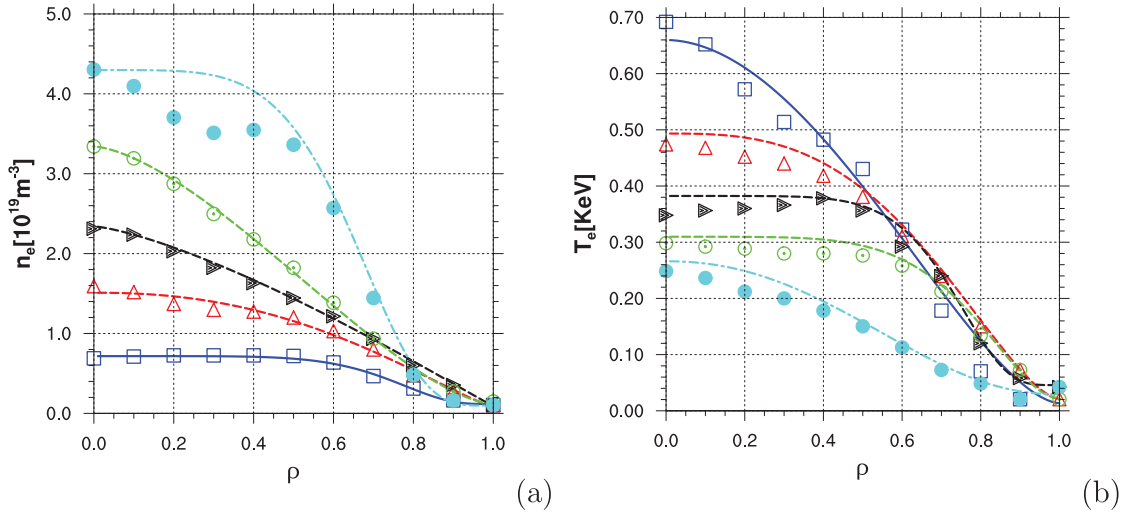
There is a known trend of smoothly decreasing central plasma potential, $\phi(0) = \phi_0$, with average density in TJ-II plasmas for all the regimes described above (LDHT, IDT and HDLT plasmas) [25]. The value ϕ_0 saturates at around -600 V for the highest densities (see shaded region in figure 7). It is worth mentioning, however, that the central electron temperature, $T_{e0} = T_e(0)$, follows an approximately inverse relation with the density, as shown in figure 3(a). Thus, the behavior of $\phi(0)$ could be partly ascribed to the electron temperature [26], but the combined dependences $\phi_0(\bar{n})$ and $T_{e0}(\bar{n})$ are a reminder of the known link between plasma potential and plasma collisionality in the theory of collisional transport.

Finally, and since an algebraic model will be used later, we have prepared a set of analytic profiles that reproduce the main features of the experimental ones shown in figure (2), having the form

Table 1. Constant values appearing in expressions (1) for different regimes of electron density and temperature (LDHT regime, IDT regime, and HDLT regime) obtained from the fitting to a hyperbolic curve $T_{e0} = 1/(0.9226 + 0.7623n_{e0})$.

	n_a	n_0	a	b	T_{ae}	T_{0e}	a_e	b_e	T_{ai}	T_{0i}	a_i	b_i
LDHT	0.11	≤ 1	6.21	4.07	0.01	(0.65, 0.7)	1.9	1.66	0.01	0.077	40	10
IDT	0.08	(1, 2)	2.27	1.23	0.02	(0.45, 0.5)	2.91	1.64	0.01	0.09	35	10
IDT	0.09	(2, 3)	1.34	1.02	0.04	(0.35, 0.4)	6.64	5.43	0.01	0.09	35	10
IDT	0.11	(3, 4)	1.53	1.58	0.02	(0.3, 0.35)	5.23	2.12	0.01	0.09	35	10
HDLT	0.09	(4, 5)	4.78	5.11	0.02	(0.25, 0.3)	2.15	2.40	0.01	0.11	30	10

Note: Densities are expressed in 10^{19} m^{-3} , and electron and ion temperatures in keV.


Figure 4. (a) Density profile and (b) electron temperature: LDHT regime (solid line) and experimental (hollow-squares), IDT regime (dashed lines) and experimental (hollow-triangles, right-pointing triangles and hollow-circles), and HDLT regime (dash-dotted line) experimental (solid-circles).

$$\begin{aligned}
 n(\rho) &= n_a + n_0(1 - \rho^a)^b; T_e(\rho) = T_{ae} + T_{0e}(1 - \rho^{a_e})^{b_e}; \\
 T_i(\rho) &= T_{ai} + T_{0i}(1 - \rho^{a_i})^{b_i},
 \end{aligned} \quad (1)$$

where n_a , T_{ae} , and T_{ai} are the electron density, electron temperature and ion temperature at the boundary, while n_0 , T_{0e} and T_{0i} give the corresponding values at the center. Since the central values of the experimental data shown in figure 2 can be well fitted by an inverse relation, $T_{e0} = 1/(0.9226 + 0.7623n_{e0})$, as seen in figure 3(a), we have taken n_0 and T_{0e} to fall on this curve. The parameters a and b in equation (1) selected for our calculations are given in table 1. They produce the profiles shown in figures 3(b) and 4, where the model profiles are compared with the experimental ones.

While most profiles are well represented by the simple binomial form of equation (1), those that are centrally peaked or slightly hollow do not have such a good fit. Although we are interested in the global features of the profiles which are enough to reproduce the basic behavior of the radial electric field profiles, as will be shown later, we can find better fits to $n(\rho)$ and $T_j(\rho)$ by superposing two binomial forms like

$$\begin{aligned}
 n(\rho) &= n_a + n_0(1 - \rho^a)^b + c(1 - \rho^d)^e; \\
 T_e(\rho) &= T_{ae} + T_{0e}(1 - \rho^{a_e})^{b_e} + c_e(1 - \rho^{d_e})^{e_e} \\
 T_i(\rho) &= T_{ai} + T_{0i}(1 - \rho^{a_i})^{b_i} + c_i(1 - \rho^{d_i})^{e_i},
 \end{aligned} \quad (2)$$

with the proper parameter choice. These better fits are shown in figure 5. However, the analytical calculations of section 4.2 show that small changes in the profiles produce correspondingly small changes in the $E_r(\rho)$ profiles except near the edge region where there is a large sensitivity in the relative values of T_e and T_i . For that reason, we show the calculations with simple profiles in order to represent the global features in the figures that follow. DKES calculations use profiles (2) as explained below.

3. Neoclassical calculations of the radial electric field

The radial electric field in a stellarator can be computed from the neoclassical transport theory, starting from the diffusive fluxes for ions and electrons, Γ_j (with $j = e, i$). These fluxes have been calculated from kinetic theory or a two-fluid description to obtain closed forms in terms of the plasma parameters by several authors [3, 27–29]. From the dependence $\Gamma_j(E_r)$ it is possible to compute the radial electric field by applying the ambipolarity condition. Here we use three different formulations of the neoclassical fluxes to obtain E_r following certain procedures that numerically integrate the analytical formulas. For the algebraic model described below, the first procedure directly solves the ambipolarity equation

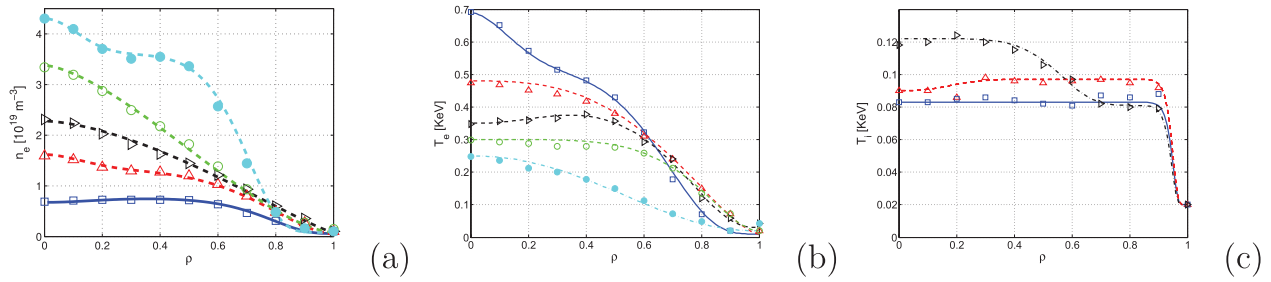


Figure 5. (a) Density profile, (b) electron temperature and (c) ion temperature profiles, using the superposition of two binomial expressions, corresponding to the same line densities as figures 3 and 4.

$$\Gamma_e(E_r) = Z_i \Gamma_i(E_r) \quad (3)$$

to determine E_r (additional conditions may be necessary if multiple roots exist for equation (3) which may produce a discontinuity of E_r as a function of the radial coordinate). The other procedure, which is more convenient from the numerical point of view, follows the evolution of the electric field solving the equation

$$\frac{\partial E_r}{\partial t} \approx \frac{|e|}{\epsilon_{\perp}} (\Gamma_e - Z_i \Gamma_i) \quad (4)$$

until a steady state is reached, which gives E_r . Here, ϵ_{\perp} is the perpendicular dielectric constant and it is assumed that a term representing electric field diffusion is small [30] (see equation (11)).

The models used in this work simplify the complicated magnetic geometry in stellarators to obtain tractable NC transport fluxes, with the consequence that the resulting formulas do not give a full account of them, but they can be used to calculate E_r . No attempt is made to match the observed radial transport since it usually has an important anomalous component, particularly in regions far away from the plasma core. Since the non-ambipolar fluxes are mainly neoclassical, we expect that the E_r obtained from NC transport explain the measured values reasonably well. The ability to reproduce the electric field should depend on the way the NC fluxes react to this field, which is different in the various models considered. The results are later compared to DKES calculations which include a detailed description of the magnetic geometry.

3.1. Semi-analytical models for the neoclassical particle fluxes

There are two ways of computing transport coefficients to obtain radial electric fields. The first one is by using a kinetic code such as DKES [31, 32] to get mono-energetic coefficients as a function of plasma collisionality and the radial electric field, and the second consists of modeling these coefficients from general physical criteria. The former is more accurate but requires more computational effort, thus we will first follow the second approach in order to show that the results obtained in a faster way can be still reasonable. For this purpose we consider three different models for describing neoclassical transport that provide analytical expressions for the particle fluxes.

3.1.1. Beidler's model. The first model provides mono-energetic transport coefficients for an idealized stellarator field with a single helical mode (see equation (5) below) obtained by Beidler [26, 33] from fits to DKES calculations. This model smoothly connects the three collisionality regimes that arise from the analytical theory of transport in a stellarator (ν , $\sqrt{\nu}$ and $1/\nu$), together with the axisymmetric transport, which becomes dominant at large collision frequencies. The mono-energetic transport coefficients have to be integrated over the thermal velocity distribution.

3.1.2. Kovrizhnykh's model. A second model reported by Kovrizhnykh [34] expresses particle fluxes, as due to the contributions of an axisymmetric part Γ_j^S and an asymmetric one Γ_j^A (i.e. non-axisymmetric) for both the electrons ($j = e$) and ions ($j = i$), $\Gamma_j = \Gamma_j^S + \Gamma_j^A$. The two parts have expressions that depend on the collisionality regime and Kovrizhnykh has derived interpolation formulas that are approximately valid for all the regimes. Formulas for the radial fluxes were given in terms of the thermodynamic forces and the magnetic helical ripple ϵ_h entering the assumed representation for the standard stellarator magnetic field with a single helical harmonic,

$$B_T = B_0(R_0/R)[1 - \epsilon_h(r) \cos(l\theta - M\varphi)]; \quad \epsilon_h(r) = \epsilon_0 I_1(Mr/R_0). \quad (5)$$

In these expressions, ϵ_0 is a constant defining the amplitude of the stellarator field, related to $\epsilon(0)$, and $I_1(x)$ is the modified Bessel function of the first kind.

The particle fluxes are based on a derivation that correctly describes the ambipolar field and the parallel (to \mathbf{B}) plasma velocity [28], and the expressions interpolated over the collisionality regimes for the symmetric and asymmetric components are listed in [34].

3.1.3. Shaing's model. There is a third model presented in [3, 27]. In these reports authors argued that several values of radial electric field that satisfy the ambipolar equation can be possible, but some of them are unstable. Thus, to find a stable solution for E_r from the thermodynamic point of view, this field must be at the minimum of the generalized heat production rate. Here, helical and toroidal ripples (ϵ_h, ϵ_t) appear explicitly in the magnetic field taken from the form $B = B_0[1 - \epsilon_t \cos\theta - \epsilon_h \cos(l\theta - m\phi)]$, which appear in the asymmetric transport fluxes [3]. The symmetric part in

this case is given by the usual expressions for axisymmetric devices [29]. The electric field is obtained by solving equation (3) with the asymmetric fluxes, which are valid in collisional and collisionless regimes since they are modified to include the $\nu^{1/2}$ regime, according to [13, 35].

The magnetic geometry in the models is taken from typical equilibrium computations and does not intend to capture the detailed geometry of the TJ-II device, although the main tendencies of collisional transport should be preserved. Profiles for the rotational transform ι and ripple amplitudes $\epsilon_{r,h}$ follow from those computations. For analytical uses the ripples are taken from the calculations in [30] which can be represented by

$$\epsilon_r = \alpha_r \rho; \quad \epsilon_h = \alpha_h 10^{\beta_h \rho}, \quad (6)$$

where the parameters α_s, β_s can be chosen to fit experimental data to account partially for geometrical effects. We found that the most appropriate value is $\alpha_r = 0.06$ for all models, but α_h and β_h are adjusted according to the model to improve the fit of the E_r profiles.

In all these models the radial electric field only enters the non-toroidally symmetric part since in a tokamak-like geometry steady state particle fluxes are ambipolar. The models are strictly valid for steady state conditions since no time dependent terms due to polarization drifts are included.

3.2. Algebraic formulation

Here we present an analytical model based on a reduced representation of Kovrizhnykh formulas, which allows us to find the roots of the ambipolar equation (3) in closed form for given plasma profiles. The process followed is to give the model profiles of equation (1) for $n(\rho), T_e(\rho)$ and $T_i(\rho)$, compute the fluxes Γ_e and Γ_i and obtain E_r from equation (3). This simplified analytical model [1] assumes a simple magnetic geometry with a single helical harmonic (i.e. equation (5)). For the helical ripple we have taken $\epsilon_h = 0.134\rho^{0.61}$ [36]. The NC fluxes used are more appropriate in a low collisionality regime where the most important contribution to the transport coefficients comes from particles locally trapped in the helical ripple wells.

It is assumed that axisymmetric and anomalous fluxes are ambipolar and then only the asymmetric contribution is relevant: $\Gamma_j = \Gamma_j^{AS}$. In a quasi-stationary state with external particle sources Γ^{ext} , the particle balance equation

$$\Gamma_j = \Gamma^{\text{ext}} \quad (7)$$

has to be solved together with the ambipolarity equation (3). But in our analytical approach, only equation (3) is considered which gives an algebraic equation of third degree in the dimensionless electric field $V = q_i E_r / T_e$. This can be solved once the equilibrium profiles $n(\rho)$ and $T_j(\rho)$ are given. However, not all profiles are physically possible, since the requirement of a single real root for V for all radial positions limits the choice of values of the profile parameters. This profile constriction can be understood, according to [1], in terms of the required particle sources obtained from equation (7) for the set of profiles

$V(\rho), n(\rho)$ and $T_j(\rho)$. When V is not real and continuous the sources are not physically acceptable and then the profiles are not actually possible. The equation for the electric field V in steady state coming from equation (3) can be written as,

$$F(\rho, V) = V^3 + b(\rho)V^2 + c(\rho)V + d(\rho) = 0, \quad (8)$$

where the coefficients $b(\rho), c(\rho)$, and $d(\rho)$ are given in [1].

Depending on the values of the coefficients $b(\rho), c(\rho)$, and $d(\rho)$, equation (8) can have up to three roots, $V_1(\rho), V_2(\rho), V_3(\rho)$. In general, when there are three roots, two of them are stable and one is unstable, so an additional criterion has to be used to decide which root actually appears (see section 3.3). For our model profiles, however, there is only a single real root for all radial positions and therefore there is no ambiguity. For arbitrarily chosen profiles, the solutions in certain regimes may present a jump in the E_r profile that corresponds to the transition from one root to another. At the root transition the electric field goes through zero and therefore the ambipolarity (equation (8)) has to be replaced by a differential equation for V , as explained in [44] (see equation (11) below). However, for our profiles in figures 3–5, this procedure is not necessary since they provide a single real root everywhere. It is important to note that the edge region is the most sensitive for yielding multiple roots, particularly at low densities, in the sense that small variations in $T_e(\rho)$ there can make a real root appear or disappear.

The profiles that have been verified to yield one real root solution for E_r all over the plasma have central values of density and electron temperature that fall on the hyperbolic curve shown in figure 3(a). This assures that the ambipolarity condition is satisfied at each magnetic surface. The density and temperature profiles corresponding to the values given in table 1, for each of the regimes defined in section 2 satisfy this criterion and are shown in figures 3(b), 4(a) and (b). The improved profile fits of figure 5 also comply with the criterion.

3.3. DKES calculations

In addition to the simple models, kinetic calculations using the DKES code have been considered in order to have a more accurate comparison point. DKES takes the magnetic geometry as obtained by the equilibrium code VMEC and follows a variational computation of the monoenergetic transport coefficients D_{ij} , obtaining minimum and maximum values for them [31, 32]. We proceed as in [45] and since only particle fluxes are needed we just focus on the coefficient D_{11} , which is calculated for a range of collisionality and E_r -field values. It is then used to obtain the thermal diffusion coefficients by averaging over a Maxwellian distribution. Then, the ion and electron fluxes are obtained by multiplying by the thermodynamic forces and the electric field is computed by solving equation (3). This is made for several radial positions in order to obtain the radial electric field profile. Near the transition point of the electron to ion roots there are typically two stable roots and the criterion for deciding which one to take is based on the minimization of the heat production rate [30, 44], which reduces to determine the sign of the integral

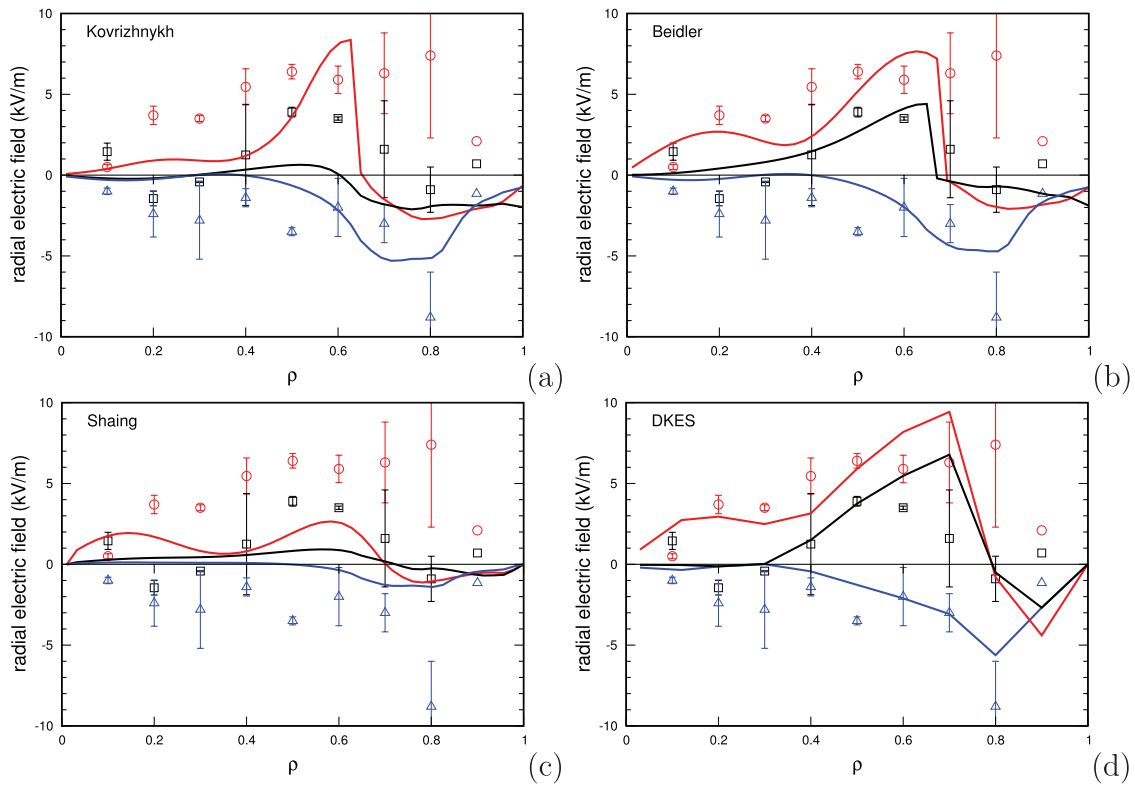


Figure 6. E_r profiles for the models of: (a) Kovrizhnykh, (b) Beidler and (c) Shaing calculated for three experimental profiles from figure 2 for different line densities corresponding to the LDHT (red lines, $\bar{n} = 0.48 \times 10^{19} \text{ m}^{-3}$), IDT (black lines, $\bar{n} = 0.95$) and HDLT (blue lines, $\bar{n} = 2.45$) regimes; experimental profiles for line densities in the same regimes are shown with symbols and error bars. (d) E_r profile from DKES for the same three densities.

$\int_{E_r^i}^{E_r^e} (\Gamma_i - \Gamma_e) dE_r$, where E_r^e and E_r^i are the electron and ion roots, respectively. When the integral is positive (negative) the ion (electron) root is selected. The values of E_r obtained with DKES are quite sensitive to the exact values of the density and the temperatures as well as their gradients. We used the fit to the experimental profiles given by equation (2) and figure 5, but the E_r profiles can be further changed by modifying the n and T_j values within the error bars seen in Figure 2.

4. Comparison with experimental data

4.1. Semi-analytical models

Here we present the results for the three models described in section 3.1. The NC particle fluxes are obtained using the formulas for each model, and the radial electric field is obtained with a numerical code coupled to the ASTRA transport shell [37] that starts with an initial E_r , normally $E_r(r) = 0$, and evolves equation (4) in every radial position r_j until a steady state is reached. When the experimental profiles of figure 2 are used the profiles obtained for the radial electric field are shown in figure 6. They are computed for three representative densities using each of the models (a, b, c), and the experimental electric field profiles are also shown for comparable densities computed from the HIBP data of the electric potential. The results from DKES are also shown for comparison (d).

The fitting to experimental profiles can be improved by varying the parameters α_h, β_h of equation (6) and it is found that $\alpha_h = 0.11$ and $\beta_h = 1.1$ produce reasonable results for Kovrizhnykh's model while Beidler's and Shaing's model results are better for $\alpha_h = 0.03$ and $\beta_h = 1.1$. This can be justified arguing that the simplification in the magnetic geometry used in the models (which is different for each one) is 'corrected for the purposes of E_r fits' with effective ripple parameters that somehow incorporate the complicated geometry of TJ-II. It is worth mentioning here that the effect of varying the effective ripple is relatively mild on E_r , while it is quite important for the particle fluxes (scaling like $\epsilon^{3/2}$ in the LMFP regime), which is due to the strong nonlinearities of the transport coefficients on the radial electric field.

As seen in figure 6, there are some general features in each density regime that reproduce those of the experimental profiles. In particular, the observed well known property of positive E_r at low density that changes to negative at large n , which is clear in figure 6, is reproduced by the theoretical models. Similar calculations were also done for the model profiles of equation (1) with equivalent results.

Since the potential is the quantity actually measured by HIBP we focus on the physical scalings of $\phi(\rho)$. The dependency with density is represented in a plot of the central potential which is the most sensitive to density. The results of the three models can be seen in figure 7 when the experimental density and temperature profiles given in figure 2 are used. It shows that the behavior of all of the models is quite similar.

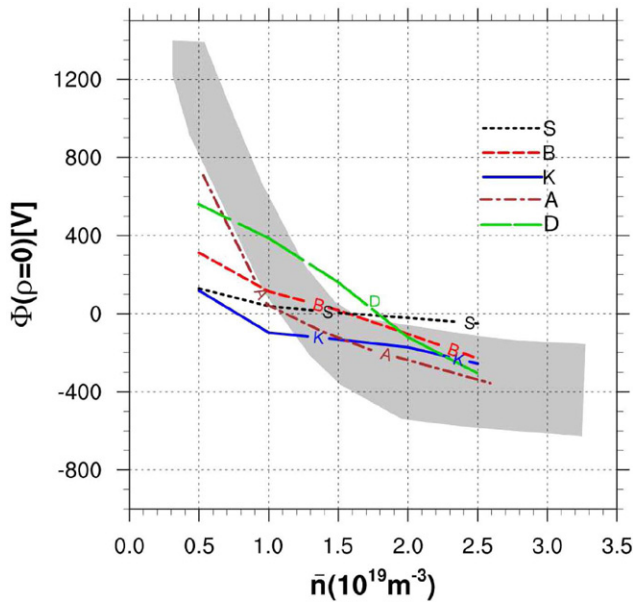


Figure 7. Plasma potential at the center obtained for Beidler (B), Kovrizhnykh (K), and Shaing (S) models using the average experimental density and temperature profiles of figure 2. The analytical result is shown by the dash-dotted line denoted by A. The shaded area shows the range covered by the experimental values [17]. DKES results are also shown (D).

We recall that the parameter ε_h has been adjusted to improve the fits in each model, thus allowing good agreement among them. The values for the algebraic computations are also shown for comparison. The shadowed region in the graph indicates the range of experimental values from HIBP and shows that the semi-analytical models are able to reproduce the measurements to some extent. At intermediate densities the agreement is good and some departure is seen for low densities due to effects not included in the NC model such as the presence of suprathermal electrons. The values of the density for the potential sign change are of the same order for all models. Shaing's model gives somewhat smaller $\phi(0)$ values. The figure also includes the results from DKES computations for which the profiles were adjusted by changing the density and temperature values within the experiment error bars tolerance in order to have a better agreement with the E_r experimental profiles. This was needed for intermediate densities to get the ion root at large radial positions. In general we found that reducing T_e or raising T_i or n produces lower values of E_r , then facilitating the appearance of the ion root. For these cases the central potential turns out to be slightly larger than the experimental range.

The results for $\phi(0)$ using the density and temperature profiles given by the models of equation (1) are shown in figure 8 but in this case ε_h was kept fixed to $\varepsilon_h = 0.134\rho^{0.61}$; for this reason the fit with Kovrizhnykh's model is not so good, being always negative. For this case it is observed that the magnitude of $\phi(0)$ is also smaller than the experimental results and the agreement between the models is not so good. It is worth mentioning that the smaller values of $|E_r|$ (and $|\phi|$) found in the HDLT case with the semi-analytical models coincides with the results found numerically based on Monte Carlo

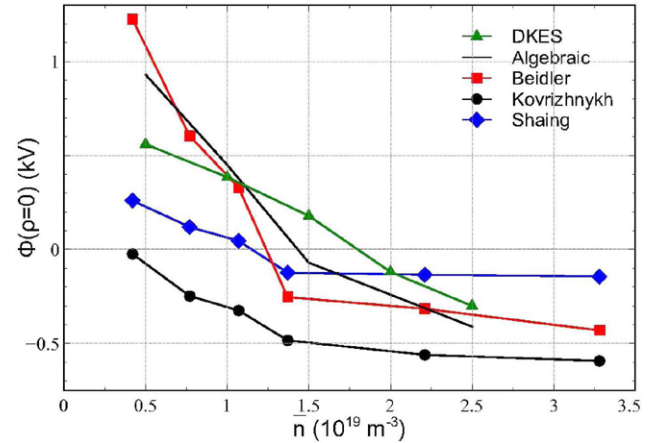


Figure 8. Electric potential at $\rho = 0$ obtained for Beidler, Kovrizhnykh, and Shaing models using the model density and temperature profiles. The result from the algebraic calculation is shown by the curve without symbols.

calculations, which also underestimate the magnitude of E_r [10]. However, it is noteworthy that the saturation of $|E_r|$ seen at high density is well reproduced by all models, although the asymptotic value is model dependent.

While the electric field from DKES is in reasonably good agreement with the simpler models, this is not necessarily the case for the particle fluxes. This is because what actually matters for the E_r profiles is the difference between electron and ion fluxes and not their absolute values. In this respect, the sensitivity of E_r mentioned before can also be understood noticing that the thermodynamic forces enter the fluxes that determine the ambipolarity condition, and these carry the detailed information about the n and T_j profiles. The monoenergetic coefficients calculated with DKES alone are not so sensitive.

4.2. Results of algebraic calculations

The roots of equation (8) provide the radial electric field profile and the plasma potential profiles, $\phi(\rho)$, are obtained from $E_r(\rho)$ after radial integration from the edge to the magnetic surface at ρ , imposing the constraint $\phi(a) = 0$. The results for the E_r -profiles in each case are shown in figure 9(a), while the plasma potential profiles are shown in figure 9(b) (see figure 1), where they are compared with experimental results from each regime. It is seen that the same general features obtained with the semi-analytical models are also reproduced, approximately matching the experimental profiles, in particular, the sign change of E_r in the IDT regime at some radial position. The electric field profiles obtained with the more accurate profiles of figure 5 are shown in figure 10. As mentioned above, the exact shape of the profiles is not too important for determining the main properties of $E_r(\rho)$, since they look similar.

A common feature already observed for TJ-II ECH plasmas [36] is that the plasma parameters for which the electric field is inverted in passing from LDHT to HDLT plasmas—the IDT regime discussed above—are found in the interval

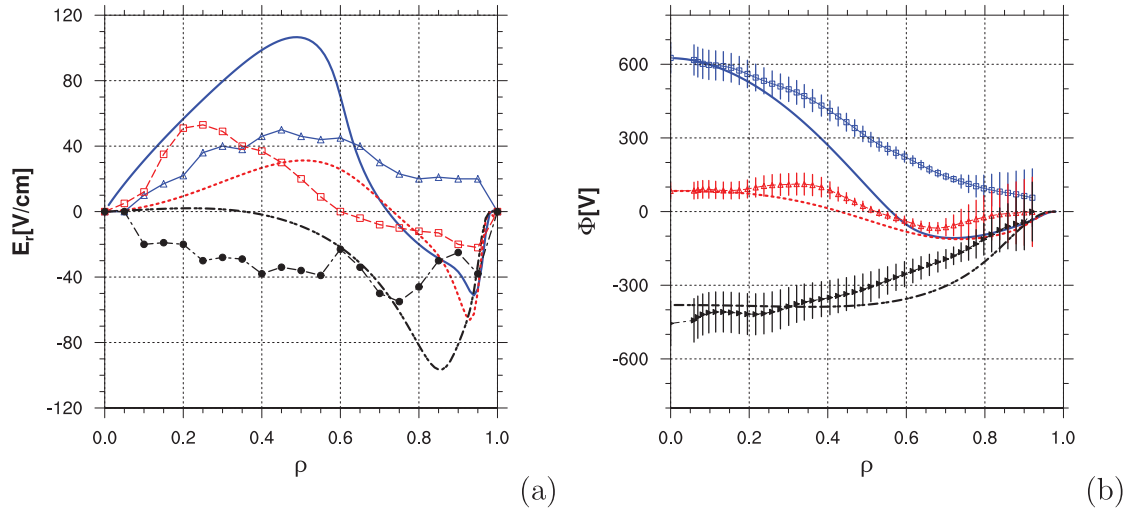


Figure 9. (a) E_r profiles from algebraic model and (b) ϕ profiles for three density model profiles LDHT (blue), IDT (red) and HDLT (black) in figures 3(b) and 4, also showing the experimental profiles from HIBP for three densities for comparison, marked with symbols [17].

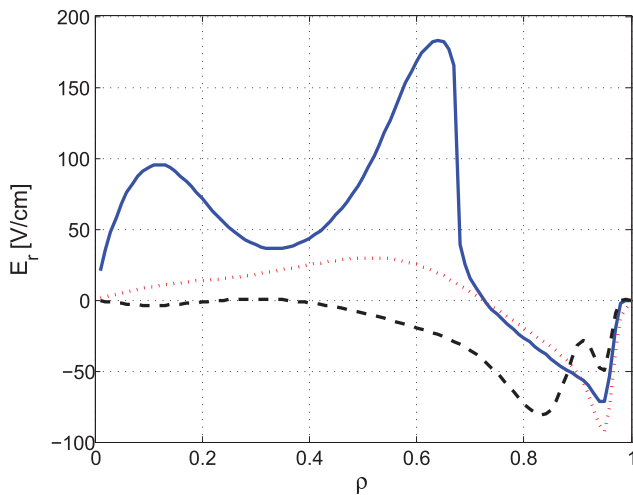


Figure 10. (a) E_r profiles from the algebraic model and for three density model profiles LDHT (blue), IDT (red) and HDLT (black) shown in figure 5.

$0.5 < (n_0/10^{19}) < 2$ in agreement with the experiments (figure 9(a)), which correspond to local collisionalities $\nu^* \sim 0.01$. It should be stressed, then, that the basic NC model, even for the complicated geometry of the TJ-II Helic-type stellarator, provides a reasonable first approximation for the main experimental results. The correlation with experimental data shown in figure 9 indicates that, although the fit is not perfect, the dependence of the plasma potential and the E_r field on the plasma parameters is consistent with NC transport (including the kinetic predictions).

5. Discussion

In light of the results obtained from our computations with the different approaches and models and compared with the HIBP measurements, we can make an appraisal of the role of NC transport regarding radial electric fields. The main results

of the comparison between experimental measurements and theoretical modeling are captured in figures 6 and 7. Figure 6 shows that both experimental and theoretical E_r -profiles approach negative values as the density increases from the lowest values; in particular, a dip in E_r begins to develop near the edge ($\rho \sim 0.8$) when n rises, prior to becoming negative (also seen in figure 9). This is systematic behavior in TJ-II plasmas that we find well described by the models. However, on the quantitative side, we find that the experimental data yields stronger fields than the models, in particular for extreme LDHT and HDLT cases. This is apparent in figure 7 for the central potential: the crossing to negative values seems reasonably well represented by the models but the high (low) potentials at low (high) density are in general underestimated. On the other hand, kinetic computations tend to have larger electric fields at intermediate densities but the values are susceptible to change when the n and T profiles are slightly modified. In this respect we must remember the simplifications of NC models that leave out some effects. In TJ-II, there are significant populations of supra-thermal electrons in LDHT conditions [38–40]. Furthermore, a low density transition to better particle confinement has been identified with the establishment of negative electric fields near the edge and the drastic drop of high energy (>20 keV) radiation from brehmstrahlung [41]. Therefore, the presence of fast electrons and ECH pump-out effects are likely candidates for explaining why the plasma electric potential presents higher $\phi(0)$ than the models where these effects are not accounted for. In the case of high density plasmas, DKES calculations which consider magnetic geometry in more detail also yield lower electric fields than measured. It has been argued that this is due to non-local effects related to large-width banana orbits for the ions in TJ-II plasmas [42, 43]. This fact might be more general according to a recent benchmarking effort between numerical NC calculations and experimental data [10]. In general, then, the semi-analytical models behave quite like the kinetic computations and other numerical results based on Monte Carlo.

Comparing the E_r profiles from the three NC models for experimental profiles (see figure 6) we notice a general agreement among them, with the Beidler and Kovrizhnykh models giving quite similar results—and reasonably close to the experimental data—and the Shaing model yielding smaller values of the electric field and plasma potential in extreme density cases. The DKES results are in better agreement with Beidler’s model, which is not surprising given that this comes from analytical fits to DKES calculations. This consistency among models together with the fair comparison with the experiment indicates the robustness of the main assumptions of NC transport, which is remarkable in the complicated geometry of the TJ-II stellarator. We point out that the experimental E_r -profiles can be better matched using $\epsilon_h(\rho)$ as a ‘fitting function’. However, the purpose of this work does not require finding a ‘best fit’ but just reasonably good behavior.

Once the NC models have been found to be a candidate for representing the radial electric field, we turn to the interpretation of some general properties of TJ-II plasmas. The transition from the LDHT regime to the IDT regime in TJ-II plasmas is characterized by a change in plasma rotation that gives rise to an $E \times B$ -flow shearing layer near the edge; in particular, the rotation velocity reverses where the electric field changes sign. We analyze this fact in terms of the plasma collisionality. In figure 11(a) the collisionality profiles are plotted for six cases of model profiles (equation (1)) from the LDHT to the HDLT regimes, and as one can see they behave differently; near the center they increase with ρ for low \bar{n} and decrease for high \bar{n} . However, the radial position where the electric field changes sign, which is marked with the lines, always falls within a limited collisionality range. The region marked with a pair of same-type lines contains the radii for E_r inversion for all density regimes for a given NC model. This region is different for each model and it can be quite large but the corresponding collisionality range is comparatively small and of similar order for all models: for the Kovrizhnykh model $0.002 < \nu^* < 0.004$, for Shaing’s $0.0033 < \nu^* < 0.0177$ and for Beidler’s $0.012 < \nu^* < 0.018$. The same pattern is observed when the experimental profiles are used for the calculation of E_r ; the ν^* profiles are shown in figure 11(b), but for these less regular profiles the results are not clear-cut, since some HDLT cases present marginal sign reversals. Excluding these non-standard cases, the collisionality range for sign reversal is seen to fall on a limited band: $0.005 < \nu^* < 0.017$, consistent with the previous cases. This means that for all profile types, when the collisionality exceeds a certain value, trapped electrons become less important than circulating ions and there is a transition from the electron to the ion root.

The agreement of the algebraic model with the semi-analytical models and the DKES results seen in figure 7 points again to the robustness of neoclassical particle fluxes in predicting electric fields. There is also a qualitative agreement for the profiles as it is clear by comparing figures 9 and 6. Therefore, we can use the algebraic formulation to study in more detail the passage from the LDHT regime to the IDT.

When a low density ECRH plasma in TJ-II evolves to a higher density via external gas puffing, the plasma rotation starts changing sign near the edge but inside the plasma [20].

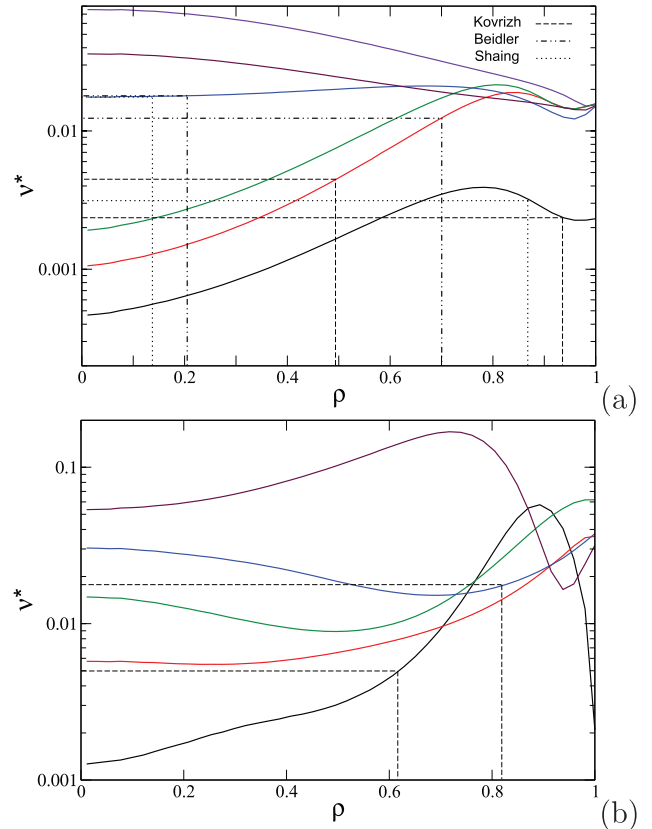


Figure 11. (a) Collisionality profiles for six model profiles ranging from low density (bottom curve) to high density (top curve), showing that the radial position range where E_r changes sign corresponds to a narrow range in collisionality that depends on the NC model used. Radial ranges for each model are marked with a pair of same-type lines which are mapped to the corresponding collision range by the appropriate density regime ($E_r < 0$ to the right of the lines). (b) Collisionality profiles for the plasma profiles in figure 2, showing the collisionality range encompassing all densities, where E_r changes sign.

To analyze this behavior, first we must note that for a given E_r , the electron and ion fluxes change with collisionality at different rates, thus, as shown above, the collision frequency should determine when and where the electric field transits from the electron root to the ion root. The plasma regions with larger collisionality should reach the ion root first. A typical observation is that the collisionality in low density plasmas shows a maximum around $\rho = 0.8$ – 0.9 as seen in figure 11 which is the same region in which E_r changes sign. Thus, we hypothesize that the collisionality maximum is what determines the radius of the E_r inversion.

This hypothesis seems to be supported by simulations of TJ-II discharge #15585 (see figure 1(a)), shown in figure 12 presenting the profile evolution of (a) the radial electric field and (b) the collisionality. For this simulation, ECE data has been used to build the evolving T_e -profile, while the density profiles have been constructed using a typical low density shape re-scaled to give the known line density. The collisionality shows a maximum near $\rho = 0.8$, which is the radial location where a dip in $E_r(\rho)$ develops and eventually becomes negative.

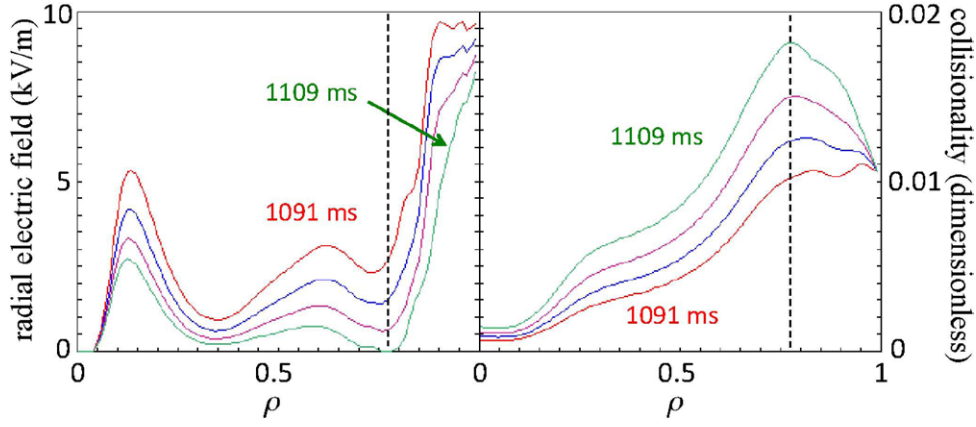


Figure 12. (a) Simulated evolution of a plasma from the LDHT to the IDT regimes where the line density evolves as in a TJ-II discharge #15585 (see figure 1(a)). The evolution of the radial electric field according to Kovrizhnykh's semi-analytical model showing that it becomes zero at $\rho \approx 0.7$. (b) Corresponding collisionality has a maximum at the same position and increases with time since density increases and the electron temperature decreases.

In order to prove this conjecture using the algebraic model it is convenient to express the asymmetric diffusion coefficients of Kovrizhnykh's algebraic model in terms of the collisionality. These coefficients are used in section 3.3 in terms of plasma density and temperatures, which follow from the monoenergetic coefficients when averaged over the thermal distributions. But, using the typical dependence of the collision frequency with density and temperature ($\nu_j \sim n/T_j^{3/2}$), the particle fluxes can be cast in terms of a normalized collision frequency, $\nu \equiv a_0 \nu_e$ (and then $\nu_i = (1/\mu a_0)(t_e/t_i)^{3/2} \nu$), as

$$\begin{aligned} \Gamma_i^{AS} &= \frac{A_i \nu L_i}{(V_i)^2 + B_i \nu^2}, & \Gamma_e^{AS} &= \frac{A_e \nu L_e}{(V_e)^2 + 0.9 \nu^2}, \\ A_i &= \rho^{3/2} n t_i^{1/2} t_e^{3/2} / a_0 \nu_0, & A_e &= \rho^{3/2} n t_e^2 \mu / a_0 \nu_0, \\ B_i &= (t_e/t_i)^3 / \mu^2. \end{aligned} \quad (9)$$

$t_j = T_j/T_0$ are normalized temperatures, $V_j = V + (q_j/q_i) \epsilon_{it} t_j$, $V = eaE_r/T_0$, $a_0 = 4.47 \times 10^{-8} \mu a$ [cm] $^2 B_0$ [T]/ T_0 [keV] ϵ_h , $\nu_e = \nu_0 \mu n t_e^{3/2}$, ν_0 [s $^{-1}$] = $316 n_0 [10^{13} \text{ cm}^{-3}] T_0$ [keV] $^{-3/2}$, $L_j = -(n'/n + b_j T_j'/T_j - q_j V/t_j q_i)$ and $\mu = 102$. These expressions have the correct dependencies $\sim \nu$ and $\sim 1/\nu$ for low and high ν , respectively and they reach a maximum value at a certain collisionality. These forms are useful for analyzing the behavior with collision frequency.

The ambipolarity condition $\Gamma_i^{AS} = \Gamma_e^{AS}$ gives the equation for the radial electric field equation (8), but now the coefficients are functions of collisionality. Therefore, the roots for the electric field $V(\nu)$ are functions of ν . From the experiment, one should expect that, for low densities, $V(\nu)$ is a decreasing function. In order to test this, we can compute $dV/d\nu$ by writing equation (8) as $F(V, \nu) = 0$ and using $dV/d\nu = -(\partial F/\partial \nu)/(\partial F/\partial V)$. The result is,

$$\frac{dV}{d\nu} = -\frac{2\nu t_i t_e^4 [V(1/t_i^{5/2} \mu + 0.9 t_e^{5/2}) t_i t_e + l_e \mu t_i^{7/2} - 0.9 l_i t_e^{7/2}]}{[3V^2 + 2b(\rho)V + c(\rho)] t_e^{1/2} + \mu l_i^{1/2}}, \quad (10)$$

with $l_j = n'/n + b_j T_j'/T_j$. When $dV/d\nu < 0$ the radial electric field drops as ν increases. This may lead to the creation of a minimum in the $E_r(\rho)$ profile where there is a maximum in the

collisionality profile $\nu(\rho)$. We have checked that $dV/d\nu \leq 0$ for all the sets of profiles considered here. This is also expected by inspecting equation (10) since the only term with positive contribution when $V > 0$ goes like $t_e^{-7/2}$ which is small for LDHT discharges. Therefore, one would expect to find a correlation between the maxima of $\nu(\rho)$ and minima of $E_r(\rho)$ based on the relation $\partial V/\partial \rho = dV/d\nu (\partial \nu/\partial \rho)$ (which holds if ν is the dominant dependence of V), as long as $dV/d\nu \neq 0$. The minimum in E_r is where it eventually reaches zero which could explain the behavior in figure 12, coincident with the collisionality maximum.

As a check for the validity of the collisionality dependencies introduced in equations (9) we have computed $\partial_\nu \Delta = \partial_\rho \Delta \partial_\nu \rho + \partial_{T_j} \Delta \partial_\nu T_j$ (with $\Delta = \Gamma_i - \Gamma_e$) directly from the full density and temperature dependencies of Kovrizhnykh, and compared it with $\partial_\nu \Delta$ computed from equation (9), with the result that the radial profiles $\partial_\nu \Delta(\rho)$ obtained using the model profiles are practically the same for the two methods. This means the assumed collisionality dependencies are appropriate and also implies that the convolution of the monoenergetic coefficients with the thermal distributions preserves the fundamental collisional dependencies.

The algebraic fluxes of equation (9) can also be used to explain the saturation of the electric field value for high densities, i.e. the ion root does not grow when higher densities are reached. By looking at the function $\Delta(\nu)$, it is noticed that $\Delta \rightarrow 0$ as $\nu \rightarrow \infty$. So, by virtue of equation (4) it implies that the electric field does not change when the density (and hence the collisionality) increases at high enough densities.

It is interesting to analyze the equilibrium point for $E_r = 0$ from the point of view of rotation dynamics. In [44] it is shown that the transition from the electron to the ion root occurs in a poloidal rotation shear layer, where E_r can be obtained from a diffusion equation which may be interpreted as a balance between the non-ambipolar flux $e(Z_i \Gamma_i - \Gamma_e)$ and a viscous particle flux, driven by a poloidal viscous force,

$$\Gamma_{\text{vis}} \equiv \frac{2}{r^2} \frac{d}{dr} \left[r^2 \hat{\eta} \left(E_r' - \frac{1}{r} E_r \right) \right] - \frac{\partial \hat{\eta}}{\partial E_r} \left(E_r' - \frac{1}{r} E_r \right)^2 = e(Z_i \Gamma_i - \Gamma_e), \quad (11)$$

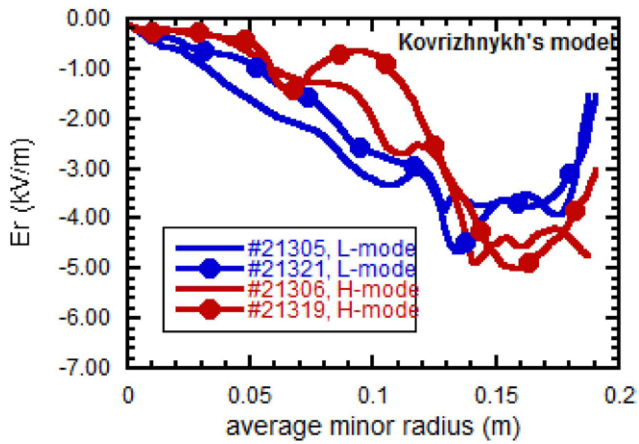


Figure 13. Electric field computed for two L-mode and the initial stage of two H-mode plasmas.

where $\hat{\eta}$ is a viscosity coefficient. From here we see that an ambipolar equilibrium ($Z_i \Gamma_i = \Gamma_e$) can be reached at a point with $\rho < 1$ for vanishing E_r , when the $E_r(\rho)$ profile has a minimum (i.e. $E_r' = 0$) there, as in the left panel of figure 12. In this case $\Gamma_{vis} = 0$, which means that the viscous stress vanishes at the point where the poloidal rotation starts to change direction. A similar result is found based on numerical calculations [46].

Finally, we turn to the problem of the formation of transport barriers in non-axisymmetric devices from the neoclassical viewpoint. In such devices the L-H transition happens at different rates, possibly due to the fact that transport barriers can develop inside the plasma (instead of right at the plasma edge, as is normally the case in tokamaks) where neoclassical fluxes are not negligible in comparison with their anomalous counterpart. Assuming the paradigm of turbulence quenching due to the establishment of sheared electric drifts, it is in order to ask whether the neoclassical electric field can provide a positive feedback loop for the establishment of a robust transport barrier. In other words, will the neoclassical E_r respond to the increasing gradients developing a stronger shearing rate in the $E \times B$ flows? This would give a positive feedback mechanism of the kind studied, e.g. in [47], where the increasing pressure gradient intensifies the shearing rate that, in turn, eases a further increment of the pressure gradient. The models used in this paper provide such positive feedback indeed. As an example, figure 13 shows a calculation using Kovrizhnykh's semi-analytical model where a stronger E_r' is found just after the L-H transition in TJ-II [2]. A deeper well in the E_r profile—and hence a stronger shearing rate—develops if the profiles are allowed to evolve under the action of a transport barrier, indicating that the neoclassical E_r can help in the process or, eventually, become the dominant feedback mechanism.

6. Conclusions

The results of calculations of the E_r field from the framework of neoclassical transport theory have been compared with experimental measurements of the plasma potential obtained

with HIBP diagnostics in the TJ-II stellarator, using simplified models and kinetic calculations based on DKES. We show that the simple models are good enough to reproduce the radial electric field, when compared with the full DKES results and with the experimental data. Different collisionality regimes were analyzed with three analytical models which *in general terms* yield E_r profiles in agreement with the experiment, indicating that neoclassical theory is one of candidates for explaining the experimental data partly based on the present analysis.

From the comparison of analytical results with those obtained from the three models considered for the neoclassical fluxes, it is noted that the Kovrizhnykh and Beidler models are more adequate for modeling non-axisymmetric NC transport in TJ-II plasmas. The Beidler model is also in good agreement with the DKES results. The qualitative agreement with experimental E_r profiles is remarkable considering that a simple magnetic geometry with a single helical harmonic was assumed for the models. The helical ripple can be adjusted to improve the fits with experimental data. Actual E_r values from DKES are quite sensitive to small variations of T_j and n profiles, especially near the plasma edge.

The good performance of the analytical NC model in predicting E_r was exploited to explain the observation that the positive E_r profile reaches zero at a point inside the plasma edge in going from LDHT to IDT regimes. It was shown that this occurs where the collision frequency profile has a maximum. It is seen from the analyzed discharge data that the collisionality maximum approximately coincides with the maximum in the pressure gradient which would explain why in [20] the velocity shear layer was identified with the maximum density gradient.

The transition from the electron to the ion root is found to occur for a certain narrow range of collisionality which points to a threshold collisionality as the cause for the transition. The implication of this is that the right amount of collisions, which destroy the trapped particle orbits that produce large electron losses, are responsible for the appearance of the ion root.

The NC model also provides support for the idea that an improved confinement mode can be maintained by the increased sheared $E \times B$ flows.

Acknowledgments

Partial support from projects PAPIIT-UNAM IN106911 and Conacyt 152905 is acknowledged. Research and data analysis of plasma electric potential done at the Kurchatov Institute was funded by Russian Scientific Foundation (Project 14-22-00193). We thank D Spong for providing an updated version of DKES.

References

- [1] Kovrizhnykh L M 2005 *Plasma Phys. Rep.* **31** 14
- [2] Estrada T *et al* 2009 *Plasma Phys. Control. Fusion* **51** 124015
- [3] Hastings D E, Houlberg W A and Shaing K C 1985 *Nucl. Fusion* **25** 445
- [4] Ida K *et al* 2003 *Phys. Rev. Lett.* **91** 085003

- [5] Fujisawa A *et al* 1999 *Phys. Rev. Lett.* **82** 2669
- [6] Stroth U *et al* 2001 *J. Plasma Fusion Res. SERIES* **4** 43
- [7] Castejon F *et al* 2002 *Nucl. Fusion* **42** 271–80
- [8] Estrada T *et al* 2006 *Fusion Sci. Technol.* **50** 127
- [9] Yokoyama M *et al* 2006 *Fusion Sci. Technol.* **50** 327
- [10] Dinklage A *et al* 2013 *Nucl. Fusion* **53** 063022
- [11] Chmyga A A *et al* 2002 *29th EPS Conf. Plasma Physics (Montreaux)* ECA vol 26B O-1.09
- [12] Hidalgo C *et al* 2005 *Nucl. Fusion* **45** S266–75
- [13] Garcia J, Dies J, Castejon F and Yamazaki K 2007 *Phys. Plasmas* **14** 102511
- [14] Vargas V I *et al* 2008 ECH power dependence of electron heat diffusion in ECH plasmas of the TJ-II stellarator *35th EPS Conf. Plasma Physics (Hersonissos)* ECA vol 32D P-5.018
- [15] Melnikov A *et al* 2011 *Nucl. Fusion* **51** 083043
- [16] Melnikov A, Hidalgo C, Ido T, Shimizu A, Fujisawa A, Dyabilin K and Lysenko S 2012 *Plasma Fusion Res.* **7** 2402114
- [17] Melnikov A V *et al* 2011 *Problems At. Sci. Technol. Series: Thermonuclear Fusion* **4** 54 (in Russian) http://vant.iterru.ru/vant_2011_3/4.pdf
- [18] Bondarenko I S *et al* 2000 *Czech. J. Phys.* **50** 1397
- [19] Tabarés F *et al* 2008 *Plasma Phys. Control. Fusion* **50** 124051
- [20] Happel T, Estrada T and Hidalgo C 2008 *Europhys. Lett.* **84** 65001
- [21] Hidalgo C, Pedrosa M A, Castellano J, van Milligen B Ph, Jiménez J A, Fraguas A L and Sánchez E 2001 *Plasma Phys. Control. Fusion* **43** A313
- [22] Baciero A, Zurro B, McCarthy K J, Burgos C and Tribaldos V 2001 *Rev. Sci. Instrum.* **72** 971–4
- [23] Herranz J *et al* 2000 *Phys. Rev. Lett.* **85** 4715
- [24] van Milligen B Ph 2011 *Rev. Sci. Instrum.* **82** 073503
- [25] Melnikov A V *et al* 2007 *Fusion Sci. Technol.* **51** 31
- [26] Maassberg H, Beidler C D and Simmet E E 1999 *Plasma Phys. Control. Fusion* **41** 1135
- [27] Shaing K C 1984 *Phys. Fluids* **27** 1567
- [28] Kovrizhnykh L M 1999 *Plasma Phys. Rep.* **25** 760
- [29] Hinton F L and Hazeline R D 1976 *Rev. Mod. Phys.* **48** 239
- [30] Turkin Yu, Beidler C D, Maassberg H, Murakami S, Tribaldos V and Wasaka A 2011 *Phys. Plasmas* **18** 022505
- [31] Hirshman S P, Shaing K C, van Rij W I, Beasley C O Jr and Crume E C 1986 *Phys. Fluids* **29** 2951
- [32] van Rij W I and Hirshman S P 1989 *Phys. Fluids B* **1** 563
- [33] Beidler C D 1996 Neoclassical transport properties of HSR *IPP-Report 2/331* p 194
- [34] Kovrizhnykh L M 2006 *Plasma Phys. Rep.* **32** 988
- [35] Crume E C, Shaing K C, Hirshman S P and Van Rij W I 1988 *Phys. Fluids* **31** 11
- [36] López-Bruna D *et al* 2010 Programas periféricos de ASTRA para el TJ-II *Informes Técnicos Ciemat* 1201
- [37] Pereverzev G V and Yushmanov P N 2002 *ASTRA: Automated System for TRansport Analysis* (Max-Planck-Institute für Plasmaphysik Rep IPP vol 5/98) (Garching: IPP)
- [38] Ochando M A *et al* 2006 *Plasma Phys. Control. Fusion* **48** 1573
- [39] Medina F *et al* 2001 *Rev. Sci. Instrum.* **72** 471
- [40] Ochando M A *et al* 2003 *Plasma Phys. Control. Fusion* **45** 221
- [41] Vargas V I *et al* 2009 Density dependence of particle transport in ECH plasmas of the TJ-II stellarator *Informes Técnicos Ciemat* 1162
- [42] López-Bruna D *et al* 2013 *Plasma Phys. Control. Fusion* **55** 015001
- [43] Velasco J L, Castejon F and Tarancon A 2009 *Phys. Plasmas* **16** 052303
- [44] Maassberg H *et al* 1993 *Phys. Fluids B* **5** 3627
- [45] Velasco J L, Castejon F 2012 *Plasma Phys. Control. Fusion* **54** 015005
- [46] Velasco J L, Alonso J A, Calvo I and Arevalo J 2012 *Phys. Rev. Lett.* **109** 135003
- [47] Carreras B A *et al* 1994 *Plasma Phys. Control. Fusion* **36** A93